# SUPPLEMENTARY MATERIAL

# Classical and Quantum Plasmonics in Graphene Nanodisks: the Role of Edge States

Thomas Christensen,[1,2] Weihua Wang,[1,2] Antti-Pekka Jauho,[2,3] Martijn Wubs,[1,2] and N. Asger Mortensen[1,2]
[1]Department of Photonics Engineering, Technical University of Denmark, DK-2800 Kgs. Lyngby, Denmark
[2]Center for Nanostructured Graphene, Technical University of Denmark, DK-2800 Kgs. Lyngby, Denmark
[3]Department of Micro- and Nanotechnology, Technical University of Denmark, DK-2800 Kgs. Lyngby, Denmark

## CONTENTS

## I. TIGHT-BINDING CALCULATIONS

### A. Atomic configuration

For definiteness, we explicate the atomic configuration considered in our Communication for tight-binding (TB) calculations. In all cases we consider the so-called carbon-carbon (CC) centered configuration [S1], wherein a carbon-carbon bond is centered at origo, see Fig. S1. Note the existence of a mixture of both zigzag- and armchair-like edge regions. In our Dirac approach we approximate this nontrivial boundary configuration by a simple zigzag boundary. Such a treatment is justified in light of the good qualitative agreement in the DOS of TB and Dirac ZZ treatments, see Fig. 2 of our Communication. Additionally, as derived by Akhmerov and Beenakker, zigzag boundary conditions result generically for non-armchair minimal lattice terminations [S2].

### B. Numerical values of physical constants

In all calculations we employ a nearest-neighbor hopping energy of $t_{\mathrm{AB}} \approx 2.8$ eV. For correspondence with results using a Dirac description we use a Fermi velocity $v_{\mathrm{F}} = \sqrt{3}a_{\mathrm{LC}}t_{\mathrm{AB}}/2\hbar \approx 0.91 \times 10^6$ m/s, where $a_{\mathrm{LC}} = 2.46$ Å denotes the lattice constant. The resulting Fermi velocity slightly overestimates the measured electronic-band velocity, $v_{\mathrm{F}}^{\mathrm{exp}} \approx 1.0 \times 10^6$ m/s, deviating from the simple linear-dispersion prediction due to the effects of many-body interactions [S3]. Nevertheless, for formal consistency within our present

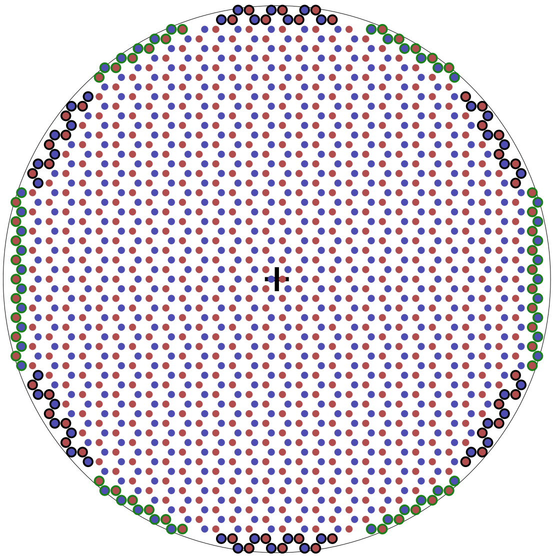

FIG. S1 CC-centered graphene disk ($R = 3.5$ nm, containing 1456 sites) with dangling bonds eliminated. A and B sublattice atoms, indicated in blue and and red, respectively, are positioned symmetrically to the left and right of origo. The presence of zigzag- and armchair-like edge regions is indicated by green and black shading, respectively.

framework, and because we choose to focus on the features associated with the Dirac Hamiltonian, we maintain $v_{\mathrm{F}} \approx 0.91 \times 10^6$ m/s throughout.

The phenomenologically introduced loss rate is chosen as $\hbar\gamma = 2\hbar\eta = 12$ meV in all calculations except in depiction of the DOS (broadened therein for clarity and to facilitate direct comparison with bulk DOS). This value is chosen to be in agreement with experimentally attained mobilities in graphene at a Fermi level near 0.4 eV, see data collected in Ref. [S4].

## II. DIRAC STATES IN DISKS

The Dirac equation, see Eq. (2), for uncoupled valleys $\kappa = \pm 1$ can be written as a two-spinor equation $\hat{\mathcal{H}}_{\mathrm{D}}^{\kappa}\boldsymbol{\psi}^{\kappa}(\mathbf{r}) = \epsilon\boldsymbol{\psi}^{\kappa}(\mathbf{r})$ which, in a polar coordinate-system $(r, \theta)$, reads as

$$\hat{\mathcal{H}}_{\mathrm{D}}^{\kappa} = -i\hbar v_{\mathrm{F}} \begin{bmatrix} 0 & \hat{L}_{-\kappa} \\ \hat{L}_{\kappa} & 0 \end{bmatrix}, \quad \text{with } \hat{L}_{\pm} = \mathrm{e}^{\pm i\theta}\Big(\partial_r \pm \tfrac{i}{r}\partial_\theta\Big). \tag{S1}$$

The corresponding solutions for systems of azimuthal symmetry take the general form [S5]:

$$\boldsymbol{\psi}_l^{\kappa}(r, \theta) = \mathrm{e}^{il\theta} \begin{bmatrix} f_l^{\mathrm{A}}(r) \\ e^{i\kappa\theta} f_{l\kappa}^{\mathrm{B}}(r) \end{bmatrix}, \quad \text{with } l \in \mathbb{Z}. \tag{S2}$$

### A. Nonzero-energy states

The explicit form of $f_l^{\mathrm{A}}(r)$ and $f_{l\kappa}^{\mathrm{B}}(r)$ is readily determined after simple manipulations of Eqs. (S1) and (S2), while enforcing regularity at the origin $r = 0$, yielding the spinor in Eq. (3), reproduced here for convenience:

$$\boldsymbol{\psi}_{ln}^{\kappa}(r, \theta) = \frac{\mathrm{e}^{il\theta}}{\sqrt{N_{ln}^{\kappa}}} \begin{bmatrix} J_l(k_{ln}^{\kappa} r) \\ i\kappa J_{l+\kappa}(k_{ln}^{\kappa} r)\mathrm{e}^{i\kappa\theta} \end{bmatrix}, \tag{S3}$$

expressed via effective momenta $k^{\kappa}_{ln} = \beta^{\kappa}_{ln}/R$ associated with nonzero energies $\epsilon^{\kappa}_{ln} = \hbar\omega_R\beta^{\kappa}_{ln}$, where $\omega_R = v_{\mathrm{F}}/R$. The normalization $N^{\kappa}_{ln}$ ensures that $\langle\boldsymbol{\psi}^{\kappa}_{ln}|\boldsymbol{\psi}^{\kappa}_{ln}\rangle = 1$, and is generally expressible as [S6, (5.54.2)]:

$$N^{\kappa}_{ln} = \pi R^2 \sum_{\zeta\in\{0,\kappa\}} \Big[J^2_{l+\zeta}(\beta^{\kappa}_{ln}) - J_{l-1+\zeta}(\beta^{\kappa}_{ln})J_{l+1+\zeta}(\beta^{\kappa}_{ln})\Big]. \tag{S4}$$

For the zigzag boundary condition (ZZ BC), which enforces $J_l(\beta_{ln}) = 0$, its form is particularly simple since Bessel zeros obey $J_{l-1}(\beta_{ln}) = -J_{l+1}(\beta_{ln})$ cf. the Bessel recursion relation $J_l(x) = \frac{x}{2l}[J_{l-1}(x) + J_{l+1}(x)]$, such that the zigzag normalization reduces to a valley-invariant form $N^{\mathrm{ZZ}}_{ln} = 2\pi R^2 J^2_{l-1}(\beta_{ln}) = 2\pi R^2 J_{l+1}(\beta_{ln})$.

## B. Zero-energy states

For zero-energy states the two-spinor equation decouples into two separate homogeneous equations $\hat{L}_{\kappa}\psi^{\kappa}_{\mathrm{A}}(r,\theta) = 0$ and $\hat{L}_{-\kappa}\psi^{\kappa}_{\mathrm{B}}(r,\theta) = 0$. Inserting the azimuthal form Eq. (S2) into these equations and solving produces solutions of the form $f^{\mathrm{A}}_l(r) = c^{\mathrm{A}}r^{\kappa l}$ and $f^{\mathrm{B}}_l(r) = c^{\mathrm{B}}r^{-(\kappa l+1)}$. Evidently, it is impossible to find normalizable solutions to the infinite mass boundary condition (IM BC), $\psi^{\kappa}_{\mathrm{B}}(R,\theta)/\psi^{\kappa}_{\mathrm{A}}(R,\theta) = i\mathrm{e}^{i\kappa\theta}$, since its enforcement would require simultaneously nonzero coefficients $c^{\mathrm{A,B}}$ [S5].

For the ZZ BC, however, we require only $\psi^{\kappa}_{\mathrm{A}}(R,\theta) = 0$, i.e. $c^{\mathrm{A}} = 0$. Regularity at the origin imposes conditions on the allowable $l$-values, which when relabeled to an integer variable $\ell$ yields the zero-energy states $\boldsymbol{\phi}^{\kappa}_{\ell}$ from Eq. (4), reproduced here for convenience [S7]:

$$\boldsymbol{\phi}^{\kappa}_{\ell}(r,\theta) = \frac{\mathrm{e}^{-i\kappa\ell\theta}}{\sqrt{\mathcal{N}_{\ell}}}\begin{bmatrix} 0 \\ r^{\ell} \end{bmatrix}, \quad \text{with } \ell = 0, 1, 2, \ldots, \ell_{\max}, \tag{S5}$$

with normalization $\mathcal{N}_{\ell} = \pi R^{2(\ell+1)}/(\ell+1)$ [in Eq. (4) of our Communication $\boldsymbol{\phi}^{\kappa}_{\ell}$ is written in terms of the dimensionless coordinate $\tilde{r} = r/R$ – as a consequence, the normalization constant associated with that form is simply $\mathcal{N}_{\ell} = \pi R^2/(\ell+1)$]. Note that, apart from the case $\ell = 0$, the states $\boldsymbol{\phi}^{\kappa}_{\ell}$ have an edge-like quality in the sense that they are localized near $r = R$, with the localization increasing with $\ell$.

### 1. Estimate of the number of zero-energy states in a zigzag-like Dirac disk

The Dirac equation, Eq. (S1), itself offers no bound on the allowable upper value of $\ell$. Nevertheless, such bounds can easily be introduced. For instance, the discreteness of the carbon lattice imposes a natural upper bound on the allowable angular momentum on the order of $\ell_{\max} \sim R/a_{\mathrm{LC}}$ [S7]. The introduction of a more precise bound, which agrees qualitatively with the above, can be facilitated by consideration of a result by Akhmerov and Beenakker. In particular, Ref. S2 demonstrates that the density of edge states per unit length of zigzag edge equals approximately $1/3a_{\mathrm{LC}}$ (including spin- and valley-degeneracies), which for a disk of circumference $2\pi R$ yields a maximal number of edge states equal to $N^{\mathrm{edge}}_{\max} = 2\pi R/3a_{\mathrm{LC}}$. Considering the range of $\ell$ in Eq. (S5) and accounting for degeneracies, it is then apparent that $\ell_{\max}$ approximately fulfills $4(\ell_{\max}+1) = N^{\mathrm{edge}}_{\max}$ for a zigzag disk.

Finally, we mention a heuristic modification applied in our calculations to the expression $N^{\mathrm{edge}}_{\max} = 2\pi R/3a_{\mathrm{LC}}$. In particular, we introduce a radial offset in the estimate of $N^{\mathrm{edge}}_{\max}$ to account for finite-size effects and the absence of edge states in TB calculations at very small radii. Specifically we find that $N^{\mathrm{edge}}_{\max} \simeq 2\pi(R-R_0)/3a_{\mathrm{LC}}$ with $R_0 = 1.5$ nm agrees well with TB calculations, see the following section, and use this estimate in calculation of $\ell_{\max}$.

### 2. Localization length of zero-energy states in Dirac disk

The degree of localization of the zero-energy states of Eq. (S5) can be investigated by assigning to each edge state of angular momentum $\ell$ a localization length $\delta R_{\ell}$, defined by the criterion:

$$\int_{R-\delta R_{\ell}\le r\le R} \mathrm{d}^2\mathbf{r}\,|\boldsymbol{\phi}^{\kappa}_{\ell}(\mathbf{r})|^2 = \text{threshold}, \tag{S6}$$

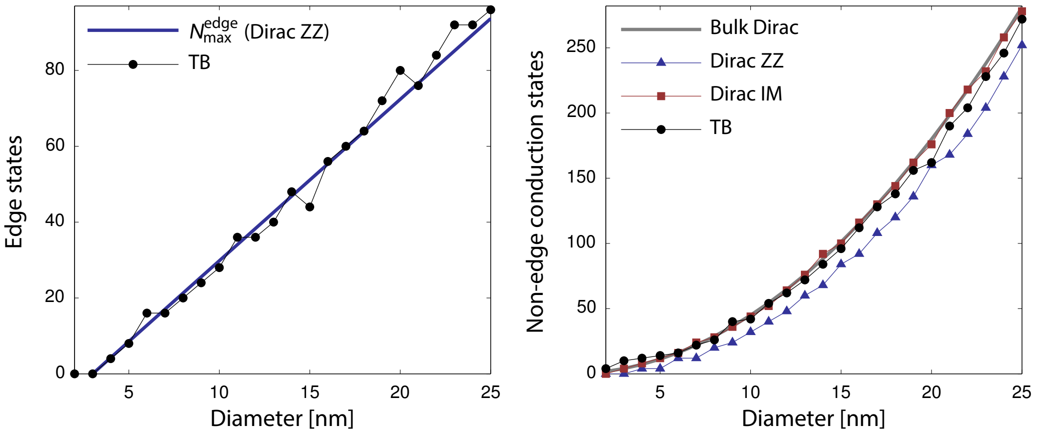

FIG. S2 Total number of edge states (left), as a function of diameter, and total number of non-edge conduction-states for a Fermi level of $\epsilon_{\text{F}} = 0.8\,\text{eV}$ (right) for a CC-centered graphene disk. The calculation of $N^{\text{edge}}_{\text{max}}$ includes the heuristic offset $R_0$ discussed in Section II.B.1.

involving a principally arbitrary threshold, which we choose as threshold $= 1 - \text{e}^{-1}$. With this definition $\delta R_\ell$ denotes the width of a two-dimensional annulus with outer radius $R$ containing precisely 50% of the mode-density. Combining Eqs. (S5) and (S6) one finds that $\delta R_\ell / R = 1 - \text{e}^{-1/2(\ell+1)}$, i.e. that the characteristic localization length depends exponentially on the angular momentum $\ell$.

### 3. Identification of edge states in tight-binding calculations

To assess the spatial character of the eigenstates of a TB calculation we introduce the participation ratio $p$ of a TB-state $\boldsymbol{\psi}$ [S8]

$$p[\boldsymbol{\psi}] = \frac{\left(\sum_n |\psi_n|^2\right)^2}{N \sum_n |\psi_n|^4}, \tag{S7}$$

where $N$ denotes the number of carbon atoms in the structure and $\psi_n$ denotes a normalized TB-state evaluated at carbon site $n$. For localized states, where only a small fraction, $N_0/N$, of carbon sites are occupied by the electron, we have $p \sim N_0/N$, while for extended states with nearly equal site occupancy we have $p \sim 1$. In practice we categorize a given state $\boldsymbol{\psi}$ as a localized edge state if $p[\boldsymbol{\psi}] < p_{\text{cut}}$ with $p_{\text{cut}} = 0.1$ (the total number of edge states being rather insensitive to this particular choice of cutoff). For the optically relevant energy-range $|\epsilon| \lesssim 2$ eV all edge states are found near the Dirac point at zero energy, albeit with a finite energy-spread. Additionally, a cluster of edge states is found near the van Hove singularity at $t_{\text{AB}} \approx 2.8$ eV which is not included in the count.

We summarize the considerations of Sections II.B.1 and II.B.3 in Fig. S2, wherein we plot the number of edge states in a zigzag Dirac treatment with cutoff $\ell_{\text{max}}$ and as estimated from a TB-treatment using the participation ratio. Additionally, we also plot the number of non-edge conduction-states, i.e. states with energy $0 < \epsilon \leq \epsilon_{\text{F}}$, and compare with ZZ and IM treatments, and also a bulk Dirac treatment with conduction electron density $n_e = \pi^{-1}(\epsilon_{\text{F}}/\hbar v_{\text{F}})^2$. A good agreement is observed across all approaches, although the zigzag Dirac treatment slightly underestimates the number of conduction electrons.

## III. NON-INTERACTING DENSITY RESPONSE OF DIRAC DISK

In this section, we present analytical expressions for the non-interacting density response function for a Dirac disk. Quite generally, we allow for the existence of nonzero-energy states $\boldsymbol{\psi}$, see Eq. (S3), and zero-energy states $\boldsymbol{\phi}$, see Eq. (S5). Expanding Eq. (5) yields two terms, one due to transitions between nonzero-energy states, $\chi^0_{\text{bulk-bulk}}$, and one due to transitions between zero- and nonzero-energy states,

$\chi^0_{\text{edge-bulk}}$ (but none from transitions between distinct zero-energy states due to Pauli blocking):

$$\chi_0(\mathbf{r},\mathbf{r}';\omega) = \chi^0_{\text{bulk-bulk}}(\mathbf{r},\mathbf{r}';\omega) + \chi^0_{\text{edge-bulk}}(\mathbf{r},\mathbf{r}';\omega), \tag{S8a}$$

$$\chi^0_{\text{bulk-bulk}}(\mathbf{r},\mathbf{r}';\omega) = 2\sum_{\kappa l n l' n'} \frac{f^{\kappa}_{ln,l'n'}}{\epsilon^{\kappa}_{ln,l'n'} - \hbar(\omega + i\eta)} \boldsymbol{\psi}^{\kappa\dagger}_{l'n'}(\mathbf{r})\boldsymbol{\psi}^{\kappa}_{ln}(\mathbf{r})\boldsymbol{\psi}^{\kappa\dagger}_{ln}(\mathbf{r}')\boldsymbol{\psi}^{\kappa}_{l'n'}(\mathbf{r}'), \tag{S8b}$$

$$\begin{aligned}\chi^0_{\text{edge-bulk}}(\mathbf{r},\mathbf{r}';\omega) = {}& 2\sum_{\kappa \ell l n} \frac{f^{\kappa}_{0,ln}}{-\epsilon^{\kappa}_{ln} - \hbar(\omega + i\eta)} \boldsymbol{\psi}^{\kappa\dagger}_{ln}(\mathbf{r})\boldsymbol{\phi}^{\kappa}_{\ell}(\mathbf{r})\boldsymbol{\phi}^{\kappa\dagger}_{\ell}(\mathbf{r}')\boldsymbol{\psi}^{\kappa}_{l'n'}(\mathbf{r}') \\ & + 2\sum_{\kappa \ell l n} \frac{f^{\kappa}_{ln,0}}{\epsilon^{\kappa}_{ln} - \hbar(\omega + i\eta)} \boldsymbol{\phi}^{\kappa\dagger}_{\ell}(\mathbf{r})\boldsymbol{\psi}^{\kappa}_{ln}(\mathbf{r})\boldsymbol{\psi}^{\kappa\dagger}_{l'n'}(\mathbf{r}')\boldsymbol{\phi}^{\kappa}_{\ell}(\mathbf{r}'),\end{aligned} \tag{S8c}$$

where $\epsilon^{\kappa}_{ln,l'n'} = \epsilon^{\kappa}_{ln} - \epsilon^{\kappa}_{l'n'}$ denotes an energy difference and $f^{\kappa}_{ln,l'n'} = f^{\kappa}_{ln} - f^{\kappa}_{l'n'}$ a population difference between states $\boldsymbol{\psi}^{\kappa}_{ln}$ and $\boldsymbol{\psi}^{\kappa}_{l'n'}$, while $f_0$ denotes a Fermi function evaluated at zero energy. The inclusion of an explicit valley summation ($\kappa$) is unnecessary for the ZZ BC, wherein the valley-degeneracy can be accounted for by a simple factor 2, but essential for the IM BC, where the valley-symmetry is broken. In the following we continue to include this explicit sum for generality.

The bulk-bulk and bulk-edge expressions can be explicated by inserting the spinors from Eqs. (S3) and Eq. (S5):

$$\chi^0_{\text{edge-bulk}}(\mathbf{r},\mathbf{r}';\omega) = 2\sum_{\kappa l n l' n'} \frac{f^{\kappa}_{ln,l'n'}}{\epsilon^{\kappa}_{ln,l'n'} - \hbar(\omega + i\eta)} \frac{\mathrm{e}^{i(l-l')(\theta-\theta')}}{N^{\kappa}_{ln}N^{\kappa}_{l'n'}} \sum_{\zeta\mu}^{\{0,\kappa\}} \mathbb{J}^{l'+\mu}_{l'+\zeta}(r,r';k^{\kappa}_{l'n'})\mathbb{J}^{l+\mu}_{l+\zeta}(r,r';k^{\kappa}_{ln}), \tag{S9a}$$

$$\chi^0_{\text{edge-bulk}}(\mathbf{r},\mathbf{r}';\omega) = 2\sum_{s=\pm1}\sum_{\kappa \ell l n} \frac{s f^{\kappa}_{ln,0}}{s\epsilon^{\kappa}_{ln} - \hbar(\omega + i\eta)} \frac{\mathrm{e}^{is(\kappa\ell + l + \kappa)(\theta-\theta')}}{N^{\kappa}_{ln}\mathcal{N}_{\ell}} (rr')^{\ell}\mathbb{J}^{l+\kappa}_{l+\kappa}(r,r';k^{\kappa}_{ln}), \tag{S9b}$$

where we have introduced short-hand notation for the double Bessel function:

$$\mathbb{J}^{t}_{q}(r,r';k) = J_q(kr)J_t(kr'). \tag{S9c}$$

Taking advantage of the azimuthal symmetry we decompose $\chi^0(\mathbf{r},\mathbf{r}';\omega)$ in angular components via

$$\chi^0(\mathbf{r},\mathbf{r}';\omega) = \sum_{m=-\infty}^{\infty} \chi^0_m(r,r';\omega)\mathrm{e}^{im(\theta-\theta')}, \tag{S10}$$

with associated parts $\chi^0_m = \chi^0_{m|\text{bulk-bulk}} + \chi^0_{m|\text{edge-bulk}}$. After some algebra [which explicitly yield selection rules $m = l - l'$ for the bulk-bulk contribution, and $m = s(\kappa\ell + l + \kappa)$ for the edge-bulk contribution] this allows us to identify the angular components as:

$$\chi^0_{m|\text{bulk-bulk}}(r,r';\omega) = 2\sum_{\kappa l n n'} \frac{f^{\kappa}_{ln,l-mn'}}{\epsilon^{\kappa}_{ln,l-mn'} - \hbar(\omega + i\eta)} \frac{1}{N^{\kappa}_{ln}N^{\kappa}_{l-mn'}} \sum_{\zeta\mu}^{\{0,\kappa\}} \mathbb{J}^{l-m+\mu}_{l-m+\zeta}(r,r';k^{\kappa}_{l-mn'})\mathbb{J}^{l+\mu}_{l+\zeta}(r,r';k^{\kappa}_{ln}), \tag{S11a}$$

$$\chi^0_{m|\text{edge-bulk}}(r,r';\omega) = 2\sum_{s=\pm1}\sum_{\kappa \ell n} \frac{s f^{\kappa}_{Ln,0}}{s\epsilon^{\kappa}_{Ln} - \hbar(\omega + i\eta)} \frac{1}{N^{\kappa}_{Ln}\mathcal{N}_{\ell}} (rr')^{\ell}\mathbb{J}^{L+\kappa}_{L+\kappa}(r,r';k^{\kappa}_{Ln}), \tag{S11b}$$

where short-hand notation $L = sm - \kappa(\ell + 1)$ is understood in the last equation.

In practical calculations we increase the maximal values of $l$, $n$, and $n'$ (up to an appropriate energy cutoff) until convergence is reached. Conversely, $\ell$ is always limited by $\ell_{\max}$ – incidentally, the resulting optical properties are relatively insensitive to small variations of $\ell_{\max}$.

## IV. EDGE-STATE CONDUCTIVITY

In this section we consider the derivation of Eqs. (8) and (9) from (6) assuming throughout a Dirac ZZ treatment (and as such, we do not allow for valley dependence in energies or occupation functions). For convenience, we reiterate the form of the local-response (LR) conductivity $\sigma(\omega)$ due to an $x$-polarized incident field:

$$\sigma(\omega) = \frac{2ie^2\omega}{\mathcal{A}} \sum_{\nu\nu'} (f_\nu - f_{\nu'}) \frac{|\langle \boldsymbol{\psi}_\nu | x | \boldsymbol{\psi}_{\nu'} \rangle|^2}{\epsilon_\nu - \epsilon_{\nu'} - \hbar(\omega + i\eta)}. \tag{S12}$$

Inserting spinors, Eq. (S3) and (S5), we find, in a similarity with the nonlocal treatment in Section III, a bulk and an edge term:

$$\sigma(\omega) = \tilde{\sigma}_{\mathrm{B}}(\omega) + \sigma_{\mathrm{E}}(\omega), \tag{S13a}$$

$$\tilde{\sigma}_{\mathrm{B}}(\omega) = \frac{2ie^2\omega}{\mathcal{A}} \sum_{\kappa l n l' n'} \frac{f_{ln,l'n'}}{\epsilon_{ln,l'n'} - \hbar(\omega + i\eta)} |\langle \boldsymbol{\psi}^\kappa_{ln} | x | \boldsymbol{\psi}^\kappa_{l'n'} \rangle|^2, \tag{S13b}$$

$$\sigma_{\mathrm{E}}(\omega) = \frac{4ie^2\omega}{\mathcal{A}} \sum_{\kappa l n \ell} \frac{f_{ln,0}\epsilon_{ln}}{\epsilon^2_{ln} - \hbar^2(\omega + i\eta)^2} |\langle \boldsymbol{\psi}^\kappa_{ln} | x | \boldsymbol{\phi}^\kappa_\ell \rangle|^2. \tag{S13c}$$

Again, no term representing transitions between distinct edge-states arise, since their distribution functions are identical and so cancel via $f_\nu - f_{\nu'} = f_0 - f_0 = 0$.

We consider in the following just the edge term $\sigma_{\mathrm{E}}(\omega)$, knowing that the term $\tilde{\sigma}_{\mathrm{B}}(\omega)$ will tend asymptotically towards the bulk infinite-extent graphene conductivity $\sigma_{\mathrm{B}}(\omega)$, see Section V. The transition matrix element can be evaluated analytically and yields:

$$\begin{aligned}
|\langle \boldsymbol{\psi}^\kappa_{ln} | x | \boldsymbol{\phi}^\kappa_\ell \rangle|^2 &\overset{\mathrm{a}}{=} \frac{\pi^2}{N_{ln}\mathcal{N}_\ell} \Big[ \sum_{s=\pm1} \delta_{l,-\kappa(\ell+1+s)} \Big] \Big| \int_0^R \mathrm{d}r\, r^{\ell+2} J_{l+\kappa}(k_{ln} r) \Big|^2 \\
&\overset{\mathrm{b}}{=} \sum_{s=\pm1} \delta_{l,-\kappa(\ell+1+s)} \frac{\pi^2}{N_{\ell+1+s,n}\mathcal{N}_\ell} \Big| \int_0^R \mathrm{d}r\, r^{\ell+2} J_{\ell+s}(k_{\ell+1+s,n} r) \Big|^2 \\
&\overset{\mathrm{c}}{=} \sum_{s=\pm1} \delta_{l,-\kappa(\ell+1+s)} \frac{\pi^2 R^{2(\ell+3)}}{N_{\ell+1+s,n}\mathcal{N}_\ell} 4\delta_{s,-1}\beta^{-4}_{\ell n} J^2_{\ell-1}(\beta_{\ell n}) \\
&\overset{\mathrm{d}}{=} 2\delta_{l,-\kappa\ell}(\ell+1)R^2\beta^{-4}_{\ell n},
\end{aligned} \tag{S14}$$

where we highlight relevant steps in the derivation in the following (which all rely on the assumption of application of the ZZ BC):

a. Orthogonality of azimuthal components. Additionally, normalization is valley-independent.
b. Generally $J_l(x) = (-1)^l J_{-l}(x)$, such that $k_{ln} = k_{-ln}$ and $N_{ln} = N_{-ln}$.
c. Use of the integral-identity $\int_0^1 \mathrm{d}\tilde{r}\, \tilde{r}^{\ell+2} J_{\ell+s}(\beta_{\ell+1+s,n}\tilde{r}) = 2\delta_{s,-1}\beta^{-2}_{\ell n} J_{\ell-1}(\beta_{\ell n})$, valid for $\beta_{\ell n}$ denoting the $n$th zero of the Bessel function $J_\ell(x)$. Identity derivable from recurrence relation for the Bessel function and the standard integral identity $\int \mathrm{d}x\, x^{p+1} J_p(x) = x^{p+1} J_{p+1}(x)$.
d. Inserting normalization constants $N_{\ell n} = 2\pi R^2 J^2_{\ell-1}(\beta_{\ell n})$ and $\mathcal{N}_\ell = \pi R^{2(\ell+1)}/(\ell+1)$.

Upon combining Eqs. (S13c) and (S14), evaluating the $\kappa$-sum (yielding a simple factor 2), and expressing all energies through $\epsilon_{\ell n} = \hbar\omega_R\beta_{\ell n}$:

$$\sigma_{\mathrm{E}}(\omega) = \frac{16ie^2}{\pi\hbar} \frac{\omega}{\omega_R} \sum_{\ell n} \frac{\ell+1}{\beta^5_{\ell n}} \frac{f_{\ell n,0}}{1 - \left(\frac{\omega+i\eta}{\beta_{\ell n}\omega_R}\right)^2}. \tag{S15}$$

In the low-temperature limit, $T \to 0$, the occupation term reduces to $f_{\ell n,0} = \theta(\hbar\omega_R\beta_{\ell n} - \epsilon_{\mathrm{F}}) - 1$, assuming $\epsilon_{\mathrm{F}} > 0$. With this simplification we readily find the result in Eq. (8) of our Communication.

### A. Large-radius asymptotic form

Rather than deal explicitly with the details of the zeros of the Bessel function, $\beta_{\ell n}$, it is convenient to note that the summation in (8) simply runs over all energies above the Fermi-level for states with angular momentum $0 \leq \ell \leq \ell_{\max}$. In the large radius limit, the energies tend to $\epsilon \simeq \hbar v_{\mathrm{F}} k$, with $k$ denoting a continuous momentum, and an associated density of states $D(\epsilon) = g_{\mathrm{d}}|\epsilon|/2\pi\hbar^2 v_{\mathrm{F}}^2$ (where $g_{\mathrm{d}} = 1$ since we have already accounted for spin- and valley-degeneracies explicitly). Ignoring the upper limit, $\ell_{\max}$, on $\ell$, which is reasonable in the large-disk case, this allows us to transform the sum via:

$$\frac{1}{\mathcal{A}}\sum_{\ell n}^{\hbar\omega_R\beta_{\ell n}\geq\epsilon_{\mathrm{F}}} \to \tfrac{1}{2}\int_{\epsilon_{\mathrm{F}}}^{\infty} \mathrm{d}\epsilon\, D(\epsilon), \tag{S16}$$

where the factor $1/2$ accounts for the fact that we only include terms $\ell \geq 0$ in the sum rather than all $l \in \mathbb{Z}$. The Bessel zeros are naturally converted via $\beta_{\ell n} \to \epsilon/\hbar\omega_R$. The remaining difficulty lies with the factor $\ell + 1$. We replace it by its average value at fixed energy, i.e. $l + 1 \to \langle l + 1\rangle_\epsilon$, which in turn can be approximated by $\langle l + 1\rangle_\epsilon \simeq \xi\epsilon/\hbar\omega_R$, where $\xi$ denotes a proportionality constant $\xi = 4/3\pi$, see Section IV.A.1.

Introducing these considerations into Eq. (8) then allows us to derive (9):

$$\begin{aligned}
\sigma_{\mathrm{E}}^{\infty}(\omega) &= \frac{-16ie^2}{\pi\hbar}\frac{\omega}{\omega_R}\frac{\xi(\hbar\omega_R)^2}{4}\int_{\epsilon_{\mathrm{F}}}^{\infty}\mathrm{d}\epsilon\,\frac{1}{\epsilon^3}\frac{1}{1-\left[\frac{\hbar(\omega+i\eta)}{\epsilon}\right]^2} \\
&= -\xi\frac{4ie^2}{\pi}\hbar\omega\omega_R\int_{\epsilon_{\mathrm{F}}}^{\infty}\mathrm{d}\epsilon\,\frac{1}{2\epsilon^2}\left[\frac{1}{\epsilon-\hbar(\omega+i\eta)}+\frac{1}{\epsilon+\hbar(\omega+i\eta)}\right] \\
&= -\xi\frac{2ie^2}{\pi}\hbar\omega\omega_R\int_{\epsilon_{\mathrm{F}}}^{\infty}\mathrm{d}\epsilon\,\frac{1}{\epsilon^2}\left[\mathcal{P}\left(\frac{1}{\epsilon-\hbar\omega}\right)+\mathcal{P}\left(\frac{1}{\epsilon+\hbar\omega}\right)+i\pi\delta(\epsilon-\hbar\omega)-i\pi\delta(\epsilon+\hbar\omega)\right] \\
&= \xi\frac{2e^2}{\pi\hbar}\frac{\omega_R}{\omega}\left[i\ln\left|\frac{\epsilon_{\mathrm{F}}^2-\hbar^2\omega^2}{\epsilon_{\mathrm{F}}^2}\right|+\pi\theta(\hbar\omega-\epsilon_{\mathrm{F}})\right],
\end{aligned} \tag{S17}$$

where we have used the identity $\frac{1}{x\pm i\eta} = \mathcal{P}\frac{1}{x} \mp i\pi\delta(x)$ valid for $\eta \to 0^+$, and that $\{\epsilon_{\mathrm{F}}, \omega\} > 0$.

### 1. Evaluation of proportionality constant $\xi$

The value of $\xi$ can be determined by considering initially the average value of $\ell$. Suppose that the probability of finding a Bessel zero $J_\ell(\beta_{\ell n}) = 0$ near some value $\epsilon/\hbar\omega_R$ is given by $P_\ell(\epsilon)$, and that the maximal $\ell$-value (after which all $P_\ell(\epsilon) = 0$) is $L$, then:

$$\langle\ell\rangle_\epsilon = \frac{\sum_{\ell=0}^{L} P_\ell(\epsilon)\ell}{\sum_{\ell=0}^{L} P_\ell(\epsilon)}. \tag{S18}$$

Evaluating this expression is straight-forward numerically. Specifically, using the following recipe one can estimate the probability $P_\ell(\epsilon)$:

1. For fixed energy $\epsilon$, and small energy-interval $\Delta\epsilon$, find all zeros, $b_j$, of the Bessel function $J_\ell(x)$ in the interval $x \in [\epsilon - \frac{1}{2}\Delta\epsilon/2, \epsilon + \frac{1}{2}\Delta\epsilon]/\hbar\omega_R$ for all $\ell = 0, 1, \ldots, L$. Denote this set as $\mathcal{B} = \{b_1, b_2, \ldots, b_M\}$, with $M$ denoting the cardinality of the set.
2. Let $\#\ell(\mathcal{B})$ denote the number of zeros in $\mathcal{B}$ of order $\ell$. The probability is then $P_\ell(\epsilon) = \#\ell(\mathcal{B})/M$.

Having computed $P_\ell(\epsilon)$ and thereby $\langle\ell\rangle_\epsilon$ the value of $\xi$ follows upon comparison with the ansatz $\langle\ell + 1\rangle_\epsilon = \langle\ell\rangle_\epsilon + 1 \simeq \xi\epsilon/\hbar\omega_R$. In Fig. S3 we show computed values of $P_\ell(\epsilon)$, averaged across bins. A clear trend is evident and indicated in dashed blue; the probability is approximately of the form $P_\ell(\epsilon) \simeq A\sqrt{1 - \ell^2/L^2}$, with $A$ being an undetermined scaling. With this form of the probability, we can approximate the expression in Eq. (S18) through the continuum limit via $\langle\ell\rangle_\epsilon \simeq \left[\int_0^L \mathrm{d}\ell\, P_\ell(\epsilon)\ell\right]/\left[\int_0^L \mathrm{d}\ell\, P_\ell(\epsilon)\right]$, where we treat $\ell$ now as a quasi-continuous variable. Evaluating this expression yields $\langle\ell + 1\rangle_\epsilon \simeq \langle\ell\rangle_\epsilon \simeq \frac{4}{3\pi}L$ (where the approximate equivalence of $\langle\ell + 1\rangle_\epsilon$ and $\langle\ell\rangle_\epsilon$ follows from our assumption of large $\epsilon/\hbar\omega_R$). Finally, we note that $L \simeq \epsilon/\hbar\omega_R$, as is also evident from Fig. S3 (this is asymptotically true for large $L$, since the first zero, $\beta_{\ell 1}$, of $J_\ell(x)$, goes like $\beta_{\ell 1} \sim \ell + O(\ell^{1/3})$ for large $\ell$, while all zeros of differing orders are bounded by $\beta_{\ell,1} < \beta_{\ell+1,1} < \ldots$[S9, (10.21.2) & (10.21.40)]). Thus, we find analytically that $\langle\ell + 1\rangle_\epsilon \simeq \xi\epsilon/\hbar\omega_R$ with $\xi = 4/3\pi$. We compare the numerical and analytical estimates in Fig. S3 and find excellent agreement across a wide range of $\epsilon/\hbar\omega_R$, improving with larger effective energies.

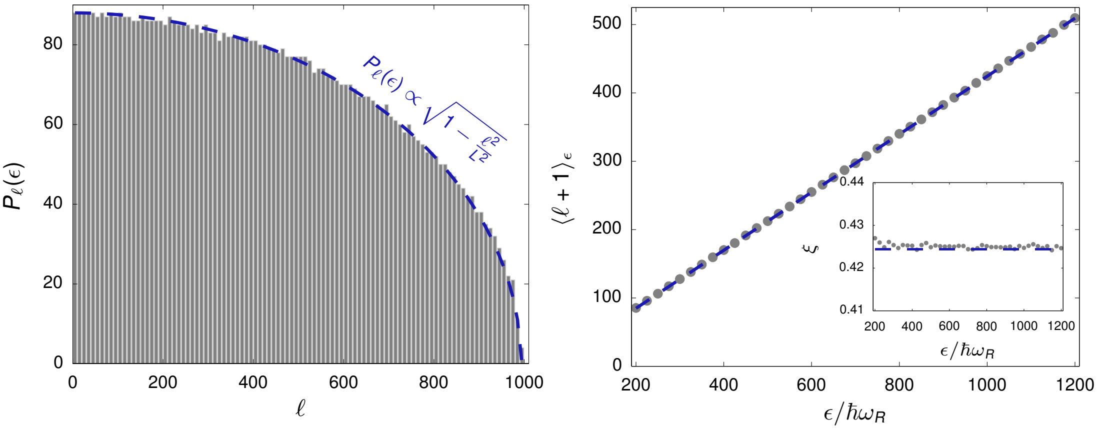

FIG. S3 Numerical and analytical considerations of the probability $P_\ell(\epsilon)$ and the proportionality constant $\xi$. Left: Probability $P_\ell(\epsilon)$ calculated numerically for $\epsilon/\hbar\omega_R = 1000$ and $\Delta\epsilon/\hbar\omega_R = 25$ with adjoining $\ell$-values collected in bins of size 10. Indicated in dashed blue is a fit $P_\ell(\epsilon) = A\sqrt{1-\ell^2/L^2}$, with $L$ denoting the maximal $\ell$-value of the computed Bessel zeros. Right: The average value $\langle \ell+1 \rangle_\epsilon$ as a function of $\epsilon/\hbar\omega_R$, computed numerically using Eq. (S18) with $\Delta\epsilon/\hbar\omega_R = 25$ and analytically via $\langle \ell+1 \rangle_\epsilon \simeq \xi\epsilon/\hbar\omega_R$ with $\xi = 4/3\pi$, in gray markers and dashed blue, respectively. Inset shows computed values of $\xi$ for different effective energies compared with the value $4/3\pi$.

## V. LOCAL-RESPONSE BULK CONDUCTIVITY

For completeness, and for comparison with the result for the edge-state conductivity, we here also give the local-response bulk conductivity, $\sigma_{\rm B}(\omega)$, utilized in Fig. 4 of our Communication. At finite temperature, $T$, the local-response intra- and interband conductivity terms in $\sigma_{\rm B}(\omega) = \sigma_{\rm intra}(\omega) + \sigma_{\rm inter}(\omega)$ are [S10]:

$$\sigma_{\rm intra}(\omega) = \sigma_0 \frac{8ik_{\rm B}T}{\pi\hbar(\omega+i\gamma)} \ln\left[2\cosh\left(\frac{\epsilon_{\rm F}}{2k_{\rm B}T}\right)\right], \tag{S19a}$$

$$\sigma_{\rm inter}(\omega) = \sigma_0\left[H(\hbar\omega/2) + \frac{4i\hbar(\omega+i\gamma)}{\pi}\int_0^\infty {\rm d}\epsilon\, \frac{H(\epsilon)-H(\hbar\omega/2)}{\hbar^2(\omega+i\gamma)^2-4\epsilon^2}\right], \tag{S19b}$$

where $\gamma = 2\eta$ denotes the optical loss-rate, $\sigma_0 \equiv e^2/4\hbar$ is a characteristic conductive magnitude, and

$$H(\epsilon) = f(-\epsilon) - f(\epsilon) = \frac{\sinh(\epsilon/k_{\rm B}T)}{\cosh(\epsilon_{\rm F}/k_{\rm B}T)+\cosh(\epsilon/k_{\rm B}T)}, \tag{S19c}$$

denotes a population difference. Following the prescription in Refs. S11 and S12 we have included phenomenological loss in both intra- and interband terms via $\gamma$. In the low-loss, low-temperature limit the terms are particularly simple, and especially the interband term is mathematically quite evocative of $\sigma_{\rm E}^\infty(\omega)$ from Eq. (S17):

$$\sigma_{\rm intra}(\omega) \overset{\gamma,T=0}{=} \sigma_0\frac{4i\epsilon_{\rm F}}{\pi\hbar\omega}, \qquad \sigma_{\rm inter}(\omega) \overset{\gamma,T=0}{=} \sigma_0\left[\frac{i}{\pi}\ln\left|\frac{2\epsilon_{\rm F}-\hbar\omega}{2\epsilon_{\rm F}+\hbar\omega}\right| + \theta(\hbar\omega-2\epsilon_{\rm F})\right]. \tag{S20}$$

## VI. LINEARIZED HYDRODYNAMIC MODEL FOR GRAPHENE

In this section we discuss the use of an approximate hydrodynamic model for graphene, and compare with the results of a small-momentum expansion of the bulk graphene density response from RPA. We also show numerically that absorption spectra calculated using Eq. (S11a) with Dirac IM states agree excellently with predictions of a hydrodynamic description in the large radius limit.

### A. Formulation of model and comparison with bulk RPA

Linearized hydrodynamic descriptions, recently widely applied to metallic systems, relate the induced current $\mathbf{J}$ and the electric field $\mathbf{E}$. For graphene, due to its two-dimensional nature, only the in-plane components of the electric field, $\mathbf{E}_\parallel$, and the surface-current $\mathbf{K}$ are of relevance. In this case, the hydrodynamic equivalent of Ohm's law (neglecting loss for the nonce) reads as [S13]:

$$\mathbf{K}(\mathbf{r},\omega) + \frac{\beta^2}{\omega^2}\nabla_\parallel[\nabla_\parallel\cdot\mathbf{K}(\mathbf{r},\omega)] = \sigma(\omega)\mathbf{E}_\parallel(\mathbf{r},\omega), \tag{S21}$$

where $\sigma(\omega)$ is a local conductivity, and $\beta$ a plasma velocity.

It is instructive to consider the resulting hydrodynamic conductivity in momentum space for longitudinal excitations $\mathbf{K}(k,\omega) = \sigma^{\mathrm{L}}_{\mathrm{H}}(k,\omega)\mathbf{E}_\parallel(k,\omega)$ where $\mathbf{k}\parallel\mathbf{E}_\parallel$:

$$\sigma^{\mathrm{L}}_{\mathrm{H}}(k,\omega) = \sigma(\omega)\Big/\Big(1-\beta^2\frac{k^2}{\omega^2}\Big) \simeq \sigma(\omega)\Big(1+\beta^2\frac{k^2}{\omega^2}\Big), \tag{S22}$$

assuming $k \ll \omega/\beta$. The values of $\beta$ and $\sigma(\omega)$ appropriate for graphene, can be discerned by comparison with the small-momentum expansion of the low-temperature nonlocal conductivity for bulk graphene $\sigma^0(k,\omega)$, whose full expression reads as [S14; S15]:

$$\sigma^0(k,\omega) = \frac{ie^2}{\pi\hbar}\frac{\tilde\omega}{\tilde k^2}\Big\{-2+\tfrac14 F(\tilde k,\tilde\omega)\Big[\mathcal{W}\Big(\frac{2+\tilde\omega}{\tilde k}\Big)-\mathcal{W}\Big(\frac{2-\tilde\omega}{\tilde k}\Big)\Big]\Big\}, \tag{S23a}$$

$$F(\tilde k,\tilde\omega) = \frac{\tilde k^2}{\sqrt{\tilde\omega^2-\tilde k^2}}\,, \qquad \mathcal{W}(x) = x\sqrt{x^2-1}-\ln\Big(x+\sqrt{x^2-1}\Big), \tag{S23b}$$

expressed in terms of normalized momenta and frequencies $\tilde k = k/k_{\mathrm{F}}$ and $\tilde\omega = \hbar\omega/\epsilon_{\mathrm{F}}$. A series expansion of this expression yields (assuming $\tilde\omega < 2$ to restrict the study to regions without Landau damping):

$$\sigma^0(k,\omega) = \underbrace{\frac{ie^2}{\pi\hbar}\frac{\epsilon_{\mathrm{F}}}{\hbar\omega}}_{\sigma_{\mathrm{intra}}(\omega)}\Big[1+\beta^2_{\mathrm{intra}}(\omega)\frac{k^2}{\omega^2}\Big] + \underbrace{\frac{ie^2}{4\pi\hbar}\ln\Big(\frac{2\epsilon_{\mathrm{F}}-\hbar\omega}{2\epsilon_{\mathrm{F}}+\hbar\omega}\Big)}_{\sigma_{\mathrm{inter}}(\omega)}\Big(1+\beta^2_{\mathrm{inter}}\frac{k^2}{\omega^2}\Big), \tag{S24a}$$

where we have indicated association with the usual local-response conductivities. The plasma velocities for the intra- and interband terms are given by:

$$\beta^2_{\mathrm{intra}}(\omega) = \Big\{\frac34 - \Big[\frac{1}{4(\epsilon_{\mathrm{F}}/\hbar\omega)^2-1}\Big]^2\Big\}v^2_{\mathrm{F}} \overset{\hbar\omega\lesssim\epsilon_{\mathrm{F}}}{\simeq} \tfrac34 v^2_{\mathrm{F}}, \qquad \beta^2_{\mathrm{inter}} = \tfrac12 v^2_{\mathrm{F}}. \tag{S24b}$$

Evidently, an appropriate hydrodynamic treatment would require a two-fluid model, accounting for the difference in plasma velocities for the intra- and interband terms. Nevertheless, a one-fluid model is reasonable, since the interband-term - and hence its nonlocal correction - is small compared to the intraband term. Hence, upon also ignoring the frequency-dispersion of $\beta_{\mathrm{intra}}$ (reasonable for disks in the large radius limit where the plasmonic resonances lie below the Fermi level), we find that Eq. (S21) with $\beta^2 = \frac34 v^2_{\mathrm{F}}$ and $\sigma(\omega) = \sigma_{\mathrm{intra}}(\omega) + \sigma_{\mathrm{inter}}(\omega)$ provides a reasonable accounting for the lowest order nonlocal corrections of the electronic plasma response.

In calculations we also account approximately for relaxation in the nonlocal part of Eq. (S21), with a rate $\gamma$, by introducing the substitutions $\beta^2 \to \frac{\omega}{\omega+i\gamma}\beta^2$ [S16; S17].

### B. Comparison of hydrodynamics and RPA with Dirac IM states

In Fig. S4 we show computational results for graphene disks of varying diameter. Very good agreement between RPA with Dirac IM states and a hydrodynamic description based on the bulk conductivity $\sigma_{\mathrm{B}}(\omega)$ is obtained, apart from the smallest considered diameter. Since RPA with Dirac IM states fully accounts for the effects of nonlocality, but completely neglects the presence of edge states, this underlines the excellent description of nonlocality by a simple hydrodynamic model with $\beta^2 = \frac34 v^2_{\mathrm{F}}$.

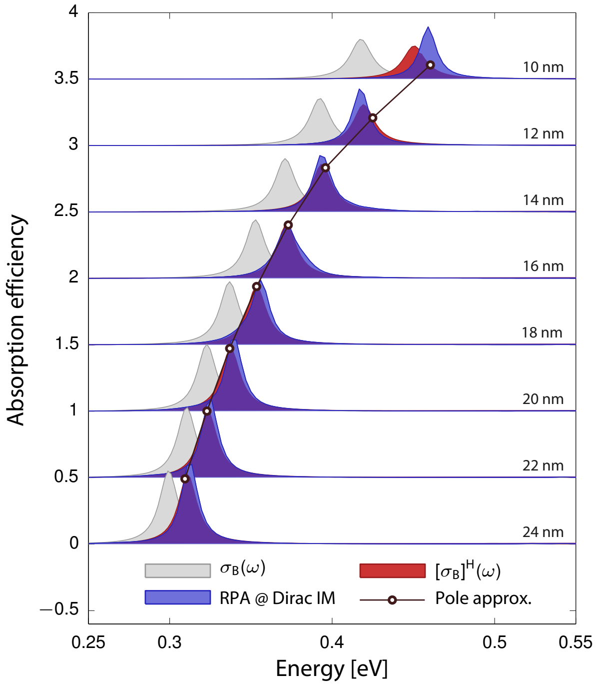

FIG. S4 Absorption cross-sectional efficiency in graphene disks, with $\epsilon_F = 0.4$ eV, $\hbar\gamma = 12$ meV, and $T = 300$ K and varying diameter (indicated above each spectra). Spectra calculated from local-response with bulk conductivity $\sigma_B(\omega)$, from hydrodynamic response with bulk conductivity (indicated in legend as $[\sigma_B]^H(\omega)$), and from RPA with Dirac IM states. A pole approximation for the spectral position of the hydrodynamic resonances is also indicated, see Eq. (S35). Spectra from different disk diameters are offset by 0.5.

## VII. ELECTROSTATIC INTERACTION IN LOCAL-RESPONSE NANODISK

A complete solution of the electrostatic problem in a two-dimensional conductive disk, accounting also for a hydrodynamic interaction in the form of Eq. (S21) and screening due to nearby grounded planes, was offered by Fetter in Ref. S18. For convenience, we repeat here the most important steps of the derivation as relevant to our case (i.e. in the absence of grounded planes). Throughout we suppress explicit declaration of frequency dependence.

The electrostatic potential, $\phi(\mathbf{r})$, is governed by the Poisson equation with a charge number density $\rho(\mathbf{r}) = \delta(z)\rho_\parallel(\mathbf{r}_\parallel)$, where $\rho_\parallel(\mathbf{r}_\parallel)$ indicates the induced in-plane charge density in the graphene sample. For a disk $\rho_\parallel(\mathbf{r}_\parallel) = \rho_\parallel(r,\theta)$ which vanishes for $r > R$. Thus;

$$\nabla^2\phi(\mathbf{r}) = -\frac{1}{\varepsilon_0\varepsilon(\mathbf{r})}\delta(z)\rho_\parallel(r,\theta), \tag{S25}$$

where we allow for a dielectric background above and below the disk via $\varepsilon(\mathbf{r}) = \varepsilon_+\theta(z) + \varepsilon_-\theta(-z)$ [and $\varepsilon(\mathbf{r}_\parallel, z = 0) = \frac{1}{2}(\varepsilon_+ + \varepsilon_-) \equiv \varepsilon_B$].

Due to the azimuthal symmetry of the disk, the potential can be decomposed in cylindrical coordinates via $\phi(\mathbf{r}) = \phi_\parallel(r)\phi_\perp(z)\mathrm{e}^{il\theta}$ [with $\phi_\perp(0) \equiv 1$], and similarly for the charge density $\rho_\parallel(\mathbf{r}_\parallel) = \rho_\parallel(r)\mathrm{e}^{il\theta}$ [we suppress explicit indication of the $l$-dependence of $\phi_\parallel(r)$, $\phi_\perp(z)$, and $\rho_\parallel(r)$ in the following, and assume it implicitly understood]. Carrying out an $l$-order Hankel transform of Eq. (S25) in coordinate $r$ allows solving for $\phi_\perp(z)$, which, through use of the boundary conditions for the potential, allows a relation between the Hankel transformed in-plane potential and charge density. By an inverse $l$-order Hankel transform of this relation one arrives at:

$$\phi_\parallel(\tilde{r}) = \frac{R}{2\varepsilon_0\varepsilon_B}\int_0^1 \mathrm{d}\tilde{r}'\, K_l(\tilde{r},\tilde{r}')\rho_\parallel(\tilde{r}')\tilde{r}', \tag{S26}$$

with kernel $K_l(\tilde{r},\tilde{r}') \equiv \int_0^\infty \mathrm{d}p\, J_l(p\tilde{r})J_l(p\tilde{r}')$, written in terms of normalized radial coordinates $\tilde{r} = r/R$.

Similarly, we can derive an additional relation between $\phi_{\parallel}$ and $\rho_{\parallel}$ by considering the hydrodynamic constitutive equation of Eq. (S21), which in the electrostatic limit is equivalent to

$$\left(1 + k_{\mathrm{NL}}^{-2}\nabla_{\parallel}^{2}\right)\rho_{\parallel}(\mathbf{r}_{\parallel}) = i\omega^{-1}\sigma\nabla_{\parallel}^{2}\phi_{\parallel}(\mathbf{r}_{\parallel}), \tag{S27}$$

with $k_{\mathrm{NL}} = \omega/\beta$, valid for $r < R$. The point at $r = R$ requires special attention: it can either be accounted for by including a Dirac delta term, $\sim \delta(r - R)$, in the constitutive equation, *or* by imposing a boundary condition at the edge. The boundary conditions of relevance is the no-spill current condition $\hat{\mathbf{r}} \cdot \mathbf{K}(r = R, \theta) = 0$ and the boundedness of $\phi_{\parallel}(r)$ and $\rho_{\parallel}(r)$. The no-spill condition can be converted to a condition on $\phi_{\parallel}(r = R)$ and $\rho_{\parallel}(r = R)$ by projecting on Eq. (S21).

Following this approach we can solve Eq. (S27) for $\phi_{\parallel}(\tilde{r})$ by using a Green function to account for the boundary condition, resulting in:

$$\phi_{\parallel}(\tilde{r}) = -i\omega\sigma^{-1}k_{\mathrm{NL}}^{-2}\rho_{\parallel}(\tilde{r}) + i\omega\sigma^{-1}R^{2}\int_{0}^{1}\mathrm{d}\tilde{r}'\, G_{l}(\tilde{r},\tilde{r}')\rho_{\parallel}(\tilde{r}')\tilde{r}', \tag{S28}$$

where $G_{l}(\tilde{r},\tilde{r}') = (2l)^{-1}[(\tilde{r}\tilde{r}')^{l} + (\tilde{r}_{<}/\tilde{r}_{>})^{l}]$ [with $\tilde{r}_{<} = \min(\tilde{r},\tilde{r}')$ and $\tilde{r}_{>} = \max(\tilde{r},\tilde{r}')$] is a Green function defined by $\Delta_{\mathrm{B}}^{l}G(\tilde{r},\tilde{r}') = -\tilde{r}^{-1}\delta(\tilde{r}-\tilde{r}')$ subject to $\partial_{\tilde{r}}G(1,\tilde{r}') = 0$ and boundedness for $\{\tilde{r},\tilde{r}'\} \in [0,1]$ (where $\Delta_{\mathrm{B}}^{l}$ denotes the Bessel differential operator of order $l$ acting on $\tilde{r}$) [S19, Section 43]. Here we have implicitly assumed that $l \neq 0$: the case of axisymmetric modes requires a separate treatment, due to the necessity of introducing an additional boundary condition which ensures that the total induced charge vanishes, see Ref. S18.

By combining Eqs. (S26) and (S28) self-consistent equations for either the in-plane potential or charge density can be found - which, in the latter case, offers:

$$\frac{\beta^{2}}{R^{2}}\rho_{\parallel}(\tilde{r}) - \omega^{2}\int_{0}^{1} G_{l}(\tilde{r},\tilde{r}')\rho_{\parallel}(\tilde{r}')\tilde{r}' + \Omega_{0}^{2}(\omega)\int_{0}^{1} K_{l}(\tilde{r},\tilde{r}')\rho_{\parallel}(\tilde{r}')\tilde{r}' = 0, \tag{S29}$$

where $\Omega_{0}^{2}(\omega) \equiv -i\omega\sigma(\omega)/2\varepsilon_{0}\varepsilon_{\mathrm{B}}R$ is a characteristic round trip frequency associated with traversal of the disk at a velocity defined by $\sigma(\omega)$ and $\varepsilon_{\mathrm{B}}$. The solution of this integral equation gives the eigenmodes, $\omega_{n}$ and $\rho_{\parallel n}(r)$, of the disk for modes of angular momentum $l$.

### A. Reduction to matrix eigenvalue problem by polynomial expansion

Rather astonishingly, the complicated integral equation in Eq. (S29) can be reduced to a matrix eigenvalue problem *with analytical matrix elements*. This fact was demonstrated in Ref. S18, by use of an expansion in a complete set of Jacobi polynomials $\{P_{j}^{l,0}(1-2\tilde{r}^{2})\}_{j=0}^{\infty}$:

$$\rho_{\parallel}(\tilde{r}) = \tilde{r}^{l}\sum_{j=0}^{\infty} c_{j}P_{j}^{l,0}(1-2\tilde{r}^{2}). \tag{S30}$$

The reduction to a matrix equation is achieved by juxtaposing $x^{l+1}P_{k}^{l,0}(1-2\tilde{r}^{2})$ onto Eq. (S29) and integrating over $\tilde{r}$, which, after utilizing the orthogonality of Jacobi polynomials, yields an algebraic equation $\sum_{j=0}^{\infty}[\frac{\beta^{2}}{R^{2}}\mathsf{D}_{jk} - \omega^{2}\mathsf{G}_{jk} + \Omega_{0}^{2}(\omega)\mathsf{K}_{jk}]c_{j} = 0$. Truncating to some cutoff $\{j,k\} = 0,1,\ldots,J$ allows reformulating this as a $J \times J$ matrix equation:

$$\left[\tfrac{\beta^{2}}{R^{2}}\mathbf{D} - \omega^{2}\mathbf{G} + \Omega_{0}^{2}(\omega)\mathbf{K}\right]\mathbf{c} = 0, \tag{S31a}$$

where the matrix elements can be evaluated exactly and take the form:

$$\mathsf{D}_{jk} = \frac{\delta_{jk}}{2(l+2j+1)}, \tag{S31b}$$

$$\mathsf{G}_{jk} = \frac{\delta_{j0}\delta_{k0}}{8l(l+1)^2} + \frac{\delta_{jk}}{4(l+2j)(l+2j+1)(l+2j+2)} + \frac{\delta_{j+1,k}+\delta_{j,k+1}}{8(l+2j+1)(l+2j+2)(l+2j+3)}, \tag{S31c}$$

$$\mathsf{K}_{jk} = \frac{(-1)^{k-j+1}}{\pi[4(k-j)^2-1](l+k+j+\frac{1}{2})(l+k+j+\frac{3}{2})}. \tag{S31d}$$

### 1. Eigenmode resonance frequencies in local-response

In the absence of nonlocality the matrix equation reduces to a generalized eigenvalue problem $\mathbf{K}\mathbf{c}_n = \zeta_n\mathbf{G}\mathbf{c}_n$ with eigenvector $\mathbf{c}_n$ and eigenvalues $\zeta_n = \omega_n^2/\Omega_0^2(\omega_n)$. The resonances can thus be categorized by the value of $\zeta_n$. In particular, the electrostatic resonances are thus governed by:

$$\frac{\omega_n}{\sigma(\omega_n)} = \frac{\zeta_n}{2i\varepsilon_0\varepsilon_{\mathrm{B}}R}, \tag{S32}$$

where the value of $l$ used in construction of $\mathbf{K}$ and $\mathbf{G}$ dictates the angular momentum of the mode, while $n$ gives its radial quantization ($n = 1, 2, \ldots$ for singly, doubly, etc.). In Table I we summarize values of $\zeta_n$ for different angular momenta and radial quantization. In the electrostatic regime, the eigenmode relevant for plane-wave interaction in nanodisks is naturally the $l = n = 1$ resonance.

| $n$ | $l = 1$ | $l = 2$ | $l = 3$ | $l = 4$ |
|---|---|---|---|---|
| 1 | 1.0977 | 1.9942 | 2.8556 | 3.7032 |
| 2 | 4.9140 | 6.2455 | 7.5124 | 8.7395 |
| 3 | 8.1337 | 9.5455 | 10.8989 | 12.2117 |
| 4 | 11.3079 | 12.7592 | 14.1596 | 15.5221 |

TABLE I Tabulated values of $\zeta_n$ for eigenmodes of angular momentum $l$ and radial quantization $n$. Calculated with a cutoff of $J = 250$, giving fully converged results accurate to last indicated decimal.

### 2. Pole approximations for hydrodynamic and edge-state conductivity contributions

Assuming that the hydrodynamic response is a small perturbation we can justify making a pole approximation to assess the impact of nonlocality. Specifically, if we indicate the local-response eigenmodes by $\omega_n^0$ and $\mathbf{c}_n^0$ the pole approximation of Eq. (S31a) becomes:

$$\left[\tfrac{\beta^2}{R^2}\mathbf{D} - \omega^2\mathbf{G} + \Omega_0^2(\omega_n^0)\mathbf{K}\right]\mathbf{c}_n = 0 \quad \Leftrightarrow \quad \tfrac{\beta^2}{R^2}\mathbf{D}\mathbf{c}_n = \omega^2\mathbf{G}\mathbf{c}_n - (\omega_n^0)^2\mathbf{G}\mathbf{c}_n^0 - \Omega_0^2(\omega_n^0)\mathbf{K}\delta\mathbf{c}_n, \tag{S33}$$

where we have used that $\Omega_0^2(\omega_n^0)\mathbf{K}\mathbf{c}_n^0 = \omega_n^0\mathbf{G}\mathbf{c}_n^0$ and also introduced the small difference $\delta\mathbf{c}_n = \mathbf{c}_n - \mathbf{c}_n^0$. Ignoring this small difference, thereby letting $\mathbf{c}_n^0 \simeq \mathbf{c}_n$, this equation can be recast as a generalized eigenvalue problem with eigenvalues $\Delta_n$:

$$\mathbf{D}\mathbf{c}_n \simeq \tfrac{R^2}{\beta^2}\left[\omega_n^2 - (\omega_n^0)^2\right]\mathbf{G}\mathbf{c}_n \equiv \Delta_n\mathbf{G}\mathbf{c}_n. \tag{S34}$$

Thus, within the pole approximation, the resonance frequency is approximately:

$$\omega_n = \sqrt{(\omega_1^0)^2 + \Delta_n\tfrac{\beta^2}{R^2}} \simeq \omega_n^0 + \frac{\Delta_n}{2\omega_n^0}\frac{\beta^2}{R^2}, \tag{S35}$$

where all the eigenvalues $\Delta_n$ are positive, leading invariably to a blueshift of the resonance, with a strength $\sim \omega_R^2/\omega_n^0$. For the optically relevant $l = n = 1$ mode we find numerically that $\Delta_1 \approx 3.39$. See Fig. S4 for an assessment of the accuracy of the approximation.

By a similar reasoning, the approximate impact of an edge-state conductivity $\sigma_{\rm E}(\omega)$ [see Eq. (S17)] can also be accounted for. Introducing again a pole approximation by letting $\sigma(\omega_n) = \sigma_{\rm B}(\omega_n) + \sigma_{\rm E}(\omega_n) \to \sigma_{\rm B}(\omega_n^0) + \sigma_{\rm E}(\omega_n^0)$ in Eq. (S32), and using Eq. (S17), one finds:

$$\omega_n \simeq \omega_n^0 + \frac{\zeta_n \sigma_{\rm E}(\omega_n^0)}{2i\varepsilon_0\varepsilon_{\rm B} R} \simeq \omega_n^0 + \frac{4\zeta_n\xi\alpha_{\rm g}}{\varepsilon_{\rm B}}\frac{\omega_R^2}{\omega_n^0}\ln\left|\frac{\epsilon_{\rm F}^2-(\hbar\omega_n^0)^2}{\epsilon_{\rm F}^2}\right|, \tag{S36}$$

where we have introduced the effective fine-structure constant for graphene $\alpha_{\rm g} = e^2/4\pi\varepsilon_0\hbar v_{\rm F} \approx 2.40$. It is evident that the edge-contribution leads to a redshift since $\mathrm{Im}[\sigma_{\rm E}(\omega_n^0)] < 0$ for $\hbar\omega_n^0 < \sqrt{2}\epsilon_{\rm F}$. Note that the strength of the hydrodynamic and edge-contribution corrections scale similarly, i.e. with $\omega_R^2/\omega_n^0$.

### B. Interaction with external potentials and the absorption cross-section

Including interaction with external potentials of definite angular momentum $l$ is straightforward. In particular, if $\phi_\parallel^{\rm ext}(\tilde{r}) = \tilde{r}^l \sum_j^\infty d_j P_j^{l,0}(1-2\tilde{r}^2)$ then the matrix system in Eq. (S31a) evolves into the inhomogeneous system:

$$\Big[\tfrac{\beta^2}{R^2}\mathbf{D} - \omega^2\mathbf{G} + \Omega_0^2(\omega)\mathbf{K}\Big]\mathbf{c} = \frac{i\omega\sigma(\omega)}{R^2}\mathbf{D}\mathbf{d}, \tag{S37}$$

The important case of the absorption cross-section, that is, the absorbed power relative to the incident intensity of a plane wave, is similarly straightforward. In particular, considering an $x$-polarized plane wave normally incident on the disk, $\mathbf{E}^{\rm ext}(\mathbf{r}_\parallel, z=0) = E_0\hat{\mathbf{x}}$, the associated electrostatic potential $\phi_\parallel^{\rm ext}(\mathbf{r}_\parallel) = -E_0 x = -\frac{1}{2}E_0 r(\mathrm{e}^{i\theta} + \mathrm{e}^{-i\theta})$, and thereby also the induced charge density, is dipolar, i.e. $l = \pm 1$. The dipole moment $\mathbf{p}(\omega)$ of the disk is just (restoring explicit frequency dependence for clarity)

$$\mathbf{p}(\omega) = \int_{r<R} \mathrm{d}^2\mathbf{r}_\parallel\, \mathbf{r}_\parallel \rho_\parallel(\mathbf{r}_\parallel, \omega) = \hat{\mathbf{x}}2\pi R^3 \int_0^1 \mathrm{d}\tilde{r}\, \tilde{r}^2 \rho_\parallel(\tilde{r}, \omega), \tag{S38}$$

where we have used that the radial charge density, $\rho_\parallel(\tilde{r}, \omega)$), is identical for $l = 1$ and $l = -1$. Using the polynomial expansion of Eq. (S30) then yields a simple connection between $\mathbf{p}(\omega) = \mathrm{p}(\omega)\hat{\mathbf{x}}$ and the expansion coefficients $\mathbf{c}(\omega)$ [S6, 7.391.3]:

$$\mathrm{p}(\omega) = 2\pi R^3 \sum_{j=0}^{\infty} c_j(\omega) \underbrace{\int_0^1 \tilde{r}^3 P_j^{1,0}(1-2\tilde{r}^2)}_{=\,\delta_{j0}/4} = \tfrac{1}{2}\pi R^3 c_0(\omega), \tag{S39}$$

with $c_0(\omega)$ obtained via Eq. (S37) with $d_j = -\frac{1}{2}E_0 R\delta_{j0}$ and $l = \pm 1$.

Finally, we note that the quasistatic polarizability relates to the dipole moment via $\alpha_0(\omega) = \mathrm{p}(\omega)/\varepsilon_0\varepsilon_{\rm B}E_0$, and that the absorption cross-section, neglecting retardation-corrections, relates to the quasistatic polarizability via $\sigma_{\rm abs}(\omega) = \frac{\omega}{c}\mathrm{Im}[\alpha_0(\omega)]$.

## VIII. ELECTROSTATIC INTERACTION IN DIRAC-RESPONSE NANODISK

The starting point for our treatment is a self-consistent equation for the induced density. In the RPA this self-consistent equation is derived by coupling the *total* potential, with contributions from both external and induced potentials $\phi = \phi^{\rm ext} + \phi^{\rm ind}$, and the induced charge density $\rho$ through the non-interacting polarizability and a Hartree interaction:

$$\rho(\mathbf{r}) = e^2 \int \mathrm{d}\mathbf{r}'\, \chi^0(\mathbf{r}, \mathbf{r}')\phi(\mathbf{r}') \tag{S40a}$$

$$\phi(\mathbf{r}) = \phi^{\rm ext}(\mathbf{r}) + \int \mathrm{d}\mathbf{r}'\, V(\mathbf{r}, \mathbf{r}')\rho(\mathbf{r}'), \tag{S40b}$$

with $V(\mathbf{r},\mathbf{r}') = 1/4\pi\varepsilon_0|\mathbf{r}-\mathbf{r}'|$ denoting the Coulomb interaction. Unlike in Section VII, all coordinates and functions refer to surface quantities, since the explicit accounting for the $z$-dimension is unnecessary. Combining these equations one readily finds integral equations for either the potential or the induced charge density. For the induced charge density, as considered also in our Communication, one finds:

$$\rho(\mathbf{r}) = e^2\int \mathrm{d}\mathbf{r}'\,\chi^0(\mathbf{r},\mathbf{r}')\left[\phi^{\mathrm{ext}}(\mathbf{r}') + \int \mathrm{d}\mathbf{r}''\,V(\mathbf{r}',\mathbf{r}'')\rho(\mathbf{r}'')\right]. \tag{S41}$$

By expanding all quantities in angular momenta,

$$\rho(r,\theta) = \sum_{m=-\infty}^{\infty}\rho_m(r)\mathrm{e}^{im\theta}, \quad \phi^{\mathrm{ext}}(r,\theta) = \sum_{m=-\infty}^{\infty}\phi_m^{\mathrm{ext}}(r)\mathrm{e}^{im\theta}, \quad V(r,r';\theta-\theta') = \sum_{m=-\infty}^{\infty}V_m(r,r')\mathrm{e}^{im(\theta-\theta')}, \tag{S42}$$

with $\chi^0(\mathbf{r},\mathbf{r}')$ expanded already in Eq. (S10), we can decouple Eq. (S41) into separate equations for each angular momentum:

$$\rho_m(\tilde{r}) = 2\pi e^2R^2\int_0^1 \mathrm{d}\tilde{r}'\,\tilde{r}'\chi_m^0(\tilde{r},\tilde{r}')\left[\phi_m^{\mathrm{ext}}(\tilde{r}') + 2\pi R^2\int_0^1 \mathrm{d}\tilde{r}''\,\tilde{r}''V_m(\tilde{r}',\tilde{r}'')\rho_m(\tilde{r}'')\right], \tag{S43}$$

expressed again in dimensionless coordinates $\tilde{r} = r/R$. The Coulomb angular elements can be read off by comparison with Eq. (S26) yielding $V_m(\tilde{r},\tilde{r}') = K_m(\tilde{r},\tilde{r}')/4\pi\varepsilon_0\varepsilon_{\mathrm{B}}R$.

The solution of this equation can be attempted e.g. via polynomial expansion - but analytical expressions for the matrix elements cannot be attained. As a consequence it is desirable to pursue a simple discretization-solution: we discretize $\tilde{r}$ by the set $\{\tilde{r}_n\}_{n=1}^{N_{\mathrm{d}}} \in [0,1]$ and find good convergence for $N_{\mathrm{d}} = 100$ in all considered cases, including in our computations also the weakly singular diagonal elements.

### A. Computational complexity and comparison with RPA at tight-binding level

The primary computational hurdle in applying RPA, both in the Dirac and the TB approaches, involves computation of $\chi^0(\mathbf{r},\mathbf{r}')$ on the set of all relevant positions $\{\mathbf{r},\mathbf{r}'\}$. We compare the complexity below:

*Tight binding* – The set $\{\mathbf{r},\mathbf{r}'\}$ is predetermined as all carbon-atom locations of which there are $N$, such that the matrix representation of $\chi^0$ has dimensions $N\times N$. Computation of the density-response at each point, i.e. of $\chi^0(\mathbf{r}_n,\mathbf{r}_{n'})$, requires $O(N^2)$ operations [cf. the double sum $\sum_{\nu\nu'}$ in Eq. (5) of our Communication]. As such, direct construction of $\chi^0$ in TB requires $O(N^4)$ operations – which, however, can be reduced to $O(N^3)$ operations by using the fast Fourier transform following the scheme suggested in Ref. [S1].

*Dirac equation* – As discussed in the previous section, the electrostatic problem can be decoupled into multipolar components $\chi_m^0$ (cf. the continuum-assumption of the Dirac equation) and the radial coordinates $(r,r')$ can subsequently be discretized e.g. on a regular grid with $N_{\mathrm{d}}$ points. Since only a single multipolar component, namely the $m=1$ ($m=-1$) component is necessary for studying interaction with plane-waves, the dimensions of the matrix representation of $\chi^0$ are just $N_{\mathrm{d}}\times N_{\mathrm{d}}$. The evaluation of $\chi_0^0(r_n,r_{n'})$ requires $O(N^\beta)$ operations, with $1<\beta<2$ [cf. the reduction of state-summations in Eq. (5) of our Communication due to the selection rules discussed in Section III], with $N$ here indicating the number of Dirac-states in the considered energy range (similar scaling as in TB). Thus, direct evaluation of $\chi_m^0$ requires $O(N_{\mathrm{d}}^2N^\beta)$.

*Self-consistent electrostatic problem* – In both cases, the self-consistent problem finally requires solving a matrix equation ($N\times N$ in TB and $N_{\mathrm{d}}\times N_{\mathrm{d}}$ in Dirac) scaling with the third power of the dimensionality by direct Gauss-Jordan elimination.

Since $N$ is on the order of several thousands, while we use $N_{\mathrm{d}} = 100$ this illustrates that application of RPA@Dirac requires significantly less computational effort compared with RPA@TB.

Of course, solving the electrostatic problem with a local conductivity $\sigma(\omega)$ is vastly simpler complexity-wise compared to RPA at any level – in particular, that problem is scale-invariant (assuming a scale-invariant conductivity). Furthermore, applying the semi-analytical solution for nanodisks discussed in Section VII requires only solving a $J\times J$ matrix equation with $J = 250$ much more than sufficient.

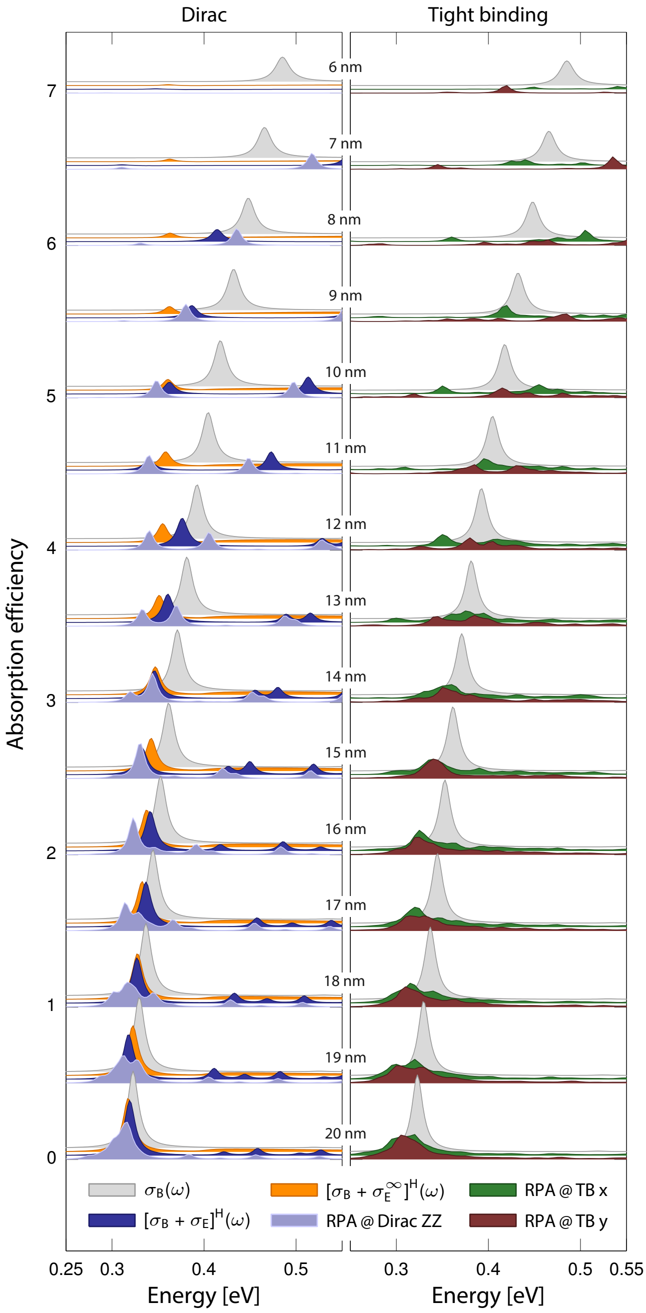

FIG. S5 Identical setup as in Fig. 4 of our Communication, but with an extended range of diameters considered. As in Fig. 4, disk-diameters are indicated above each spectra, with different diameters offset by 0.5, while individual spectra at identical diameters are offset by 0.025.

## IX. ABSORPTION SPECTRA AT INTERMEDIATE AND SMALLER DIAMETERS

In support of Fig. 4 of our Communication, we here offer additional data in Fig. S5, adding to Fig. 4 absorption spectra at intermediate diameters, as well as considering also smaller diameters. The spectra at intermediate diameters follow the trends also observed in Fig. 4. At very small diameters, predictions of the spectral position of resonances in both local and Dirac approaches are unable to match those of TB – and the polarization-dependence becomes even more pronounced – highlighting the necessity for atomistic treatments in this size-range. Nevertheless, one feature qualitatively reproduced by both edge-corrected LR and Dirac approaches at very small diameters is a dramatically reduced absorption efficiency, not captured by a bulk LR approach. This reduction sets in as the resonances move into the region of edge-to-bulk EHP transitions. In fact, the overall reduction is slightly overestimated in Dirac and edge-corrected LR since the Dirac approach overestimates the energy-level spacing due to assumed azimuthal and valley symmetry which is not present in a TB treatment.

## References

[S1] S. Thongrattanasiri, A. Manjavacas, and F.J. García de Abajo, ACS Nano **6**, 1766 (2012).
[S2] A.R. Akhmerov and C.W.J. Beenakker, Phys. Rev. B **77**, 085423 (2008).
[S3] A.H. Castro Neto, F. Guinea, N.M.R. Peres, K.S. Novoselov, and A.K. Geim, Rev. Mod. Phys. **81**, 109 (2009).
[S4] P. Tassin, T. Koschny, and C.M. Souloulis, Science **341**, 620 (2013).
[S5] M. Grujić, M. Zarenia, A. Chaves, M. Tadić, G.A. Farias, and F.M. Peeters, Phys. Rev. B **84**, 205441 (2011).
[S6] I.S. Gradshteyn and I.M. Ryzhik, *Table of integrals, series, and products*, 7th ed. (Academic Press, 2007).
[S7] B. Wunsch, T. Stauber, and F. Guinea, Phys. Rev. B **77**, 035316 (2008).
[S8] M. Wimmer, A.R.. Akhmerov, and F. Guinea, Phys. Rev. B **82**, 045409 (2010).
[S9] National Institute of Standards and Technology, "Digital library of mathematical functions," Release 1.0.8 of 2014-04-25.
[S10] L.A. Falkovsky and A.A. Varlamov, Eur. Phys. J. B **56**, 281 (2007).
[S11] V.P. Gusynin, S.G. Sharapov, and J.P. Carbotte, J. Phys.: Condens. Matter **19**, 026222 (2007).
[S12] G.W. Hanson, J. Appl. Phys. **104**, 084314 (2008).
[S13] W. Wang and J.M. Kinaret, Phys. Rev. B **87**, 195424 (2013).
[S14] B. Wunsch, T. Stauber, F. Sols, and F. Guinea, New J. Phys. **8**, 318 (2006).
[S15] E.H. Hwang and S. Das Sarma, Phys. Rev. B **75**, 205418 (2007).
[S16] P. Halevi, Phys. Rev. B **51**, 7497 (1995).
[S17] S. Raza, G. Toscano, A.-P. Jauho, M. Wubs, and N.A. Mortensen, Phys. Rev. B **84**, 121412(R) (2011).
[S18] A.L. Fetter, Phys. Rev. B **33**, 5221 (1986).
[S19] A.L. Fetter and J.D. Walecka, *Theoretical Mechanics of Particles and Continua* (Dover Publications, 1980).